Measurements of the Internal Structure of Gas-Liquid Plumes

Y.Y. SHENG and G.A. IRONS

Gas injection into liquid metals has been studied extensively with gas injection into water models. While the general features of such flows are appreciated, the structure of the two-phase region has not been well characterized. To improve our understanding of the fundamental transport phenomena in the two-phase region, a combined laser Doppler anemometry (LDA) and electrical probe (EP) technique has been developed to measure the time-averaged and fluctuating liquid velocities, bubble velocities, and void fraction. The primary findings are: (1) The slip velocity of the bubbles is close to the terminal rising velocity of bubbles in stagnant fluids. (2) The intensity of turbulence in the two-phase region is generally higher than 0.5, which is higher than in the single-phase region. (3) The turbulence is not isotropic; it is greater in the vertical direction. The implications for mathematical modeling and process analysis are discussed.

I. INTRODUCTION

GAS injection is widely practiced in the metallurgical industry for converting, refining, temperature and composition homogenization, and inclusion flotation. There has been a great deal of work performed on water models of the various injection processes in order to understand the fluid mechanics associated with gas injection. One of the major achievements of such studies has been the measurement of the liquid velocity in the single-phase region. Furthermore, complementary mathematical models of the turbulent, recirculatory flow in the single-phase regions can account for the observations quite well. The nature of the flow in the two-phase region is not understood in detail, principally because the measurement of gas and liquid velocities and phase fractions is more difficult. Furthermore, the mathematical modeling of turbulent, two-phase flow is at a more rudimentary stage of development. Nevertheless, a detailed description of the two-phase region is necessary to understand the exchanges of momentum, heat, and mass in injection systems.

Several techniques have been used to investigate the nature of flow in the two-phase region. Electrical probes (EPs) have been used extensively for the measurement of void fraction and bubble frequency distributions.[1,2,3] Information on bubble rising velocity can also be obtained with a modified probe having double tips aligned in the direction of the bubble rise.[4,5,6] Electrical probes of this type cannot be used to measure the liquid velocity.

Velocity measurements have been performed with a variety of techniques, such as cinematographic observation of the motion of tracer particles of the liquid flow field,[7] video flow visualization and laser Doppler anemometry (LDA) measurement of the liquid flow,[8,9] and the hot film anemometry of the liquid velocities.[10] Strictly speaking, the latter two techniques are limited to velocity measurements in liquid phase, unless special precautions are taken to identify the individual phases. Nevertheless, efforts have been made to obtain velocity information from inside the two-phase zone. Grevet *et al.* used LDA to obtain velocity data inside the plume zone.[9] They did not mention any specific procedures for discrimination of the velocity data from the gas and liquid phases, so the measured velocities were a mixture of gas and liquid velocities, probably skewed to the liquid phase. In the work performed by Oeters *et al.*,[10] the velocity signals from the gas phase may have been eliminated because the cooling effect caused by bubbles to the hot film is rather weak; as a result, most of their data probably originated from the liquid phase. Anagbo and Brimacombe developed a new approach by measuring the liquid velocity in the single-phase zone with an LDA and measuring the bubble velocity in the plume zone with an electrical probe;[11] they made no liquid velocity measurements in the two-phase region. Johansen *et al.* measured liquid velocities in the whole flow domain with an LDA, eliminating bubble signals by assuming that all the signals from the bubbles had much stronger intensities and could be eliminated by setting a maximum threshold for the photomultiplier tube.[12] This procedure is not always correct, since a large fraction of the signals from bubbles is not significantly stronger than the signals from the liquid.[13] Consequently, their velocities in the plume zone are expected to be a mixture from both phases.

To summarize, there has been no reliable technique developed to discriminate between the gas and liquid velocities in the plume, and moreover, simultaneous void fraction measurements are required to fully characterize the two-phase flow. The lack of such experimental data has severely limited progress in mathematical modeling. The aim of the present article is, therefore, to analyze the turbulent characteristics of the liquid flow in the plume zone and the relative velocity between the bubbles and the liquid phase based on the experimental results obtained with a combined LDA and EP technique.

II. PRINCIPLES OF TWO-PHASE VELOCITY SEPARATION

The major difficulty encountered in the measurement of velocity in two-phase flows is the separation of velocity signals of the liquid phase from those of the gas

Y.Y. SHENG, Postdoctoral Fellow, and G.A. IRONS, Professor and Chairman, are with the Department of Materials Science and Engineering, McMaster University, Hamilton, ON L8S 4L7, Canada.

Manuscript submitted March 24, 1992.

phase. A review and discussion of the many approaches developed to tackle the problem have been presented elsewhere.[13] The major conclusions are summarized below.

In general, the flow regime may be divided into three categories in terms of the combined gas and liquid velocity probability distribution function (PDF), as follows:

(1) The PDF of the velocity mixture clearly demonstrates two separate peaks representing the gas and liquid velocity distributions (Figure 1(a)). This occurs when small bubbles (less than 5-mm diameter) rise in single file with a low level of turbulence. The velocities of the two phases can be separated easily by setting a threshold between the two peaks.

(2) The two peaks of the mixed velocity PDF partially overlap each other, which makes the determination of the threshold value difficult (Figure 1(b)). More sophisticated data processing techniques are required to separate the velocities. By assuming that the PDF of each phase is Gaussian and is independent of the other, a statistical procedure has been developed to separate the two PDFs.[13]

(3) The combined PDFs of the two phase velocities merge almost completely (Figure 1(c)). This takes place in most bubbly two-phase flows with large bubble sizes, high void fractions, and high turbulent intensities, characteristic of water models of ladle metallurgy processes. The simultaneous measurement of both liquid- and gas-phase velocities can be achieved with a combined laser Doppler anemometer and EP technique. At the point where the velocity is to be measured, the LDA is first focused, and the EP tip is positioned as close to the focus as possible so that the acquisition of signals from LDA and EP is from virtually the same measuring point. The function of the EP is twofold. It measures the void fraction and bubble frequency, as well as differentiates the LDA bubble velocity signals from the liquid ones.[13]

The techniques for two-phase velocity separation have been employed in the present study to obtain velocities of both the liquid phase and the bubble phase, together with the distributions of the void fraction and the bubble frequency. These experimental results are analyzed to yield additional understanding of the turbulent nature of the two-phase flow in ladle metallurgy processes.

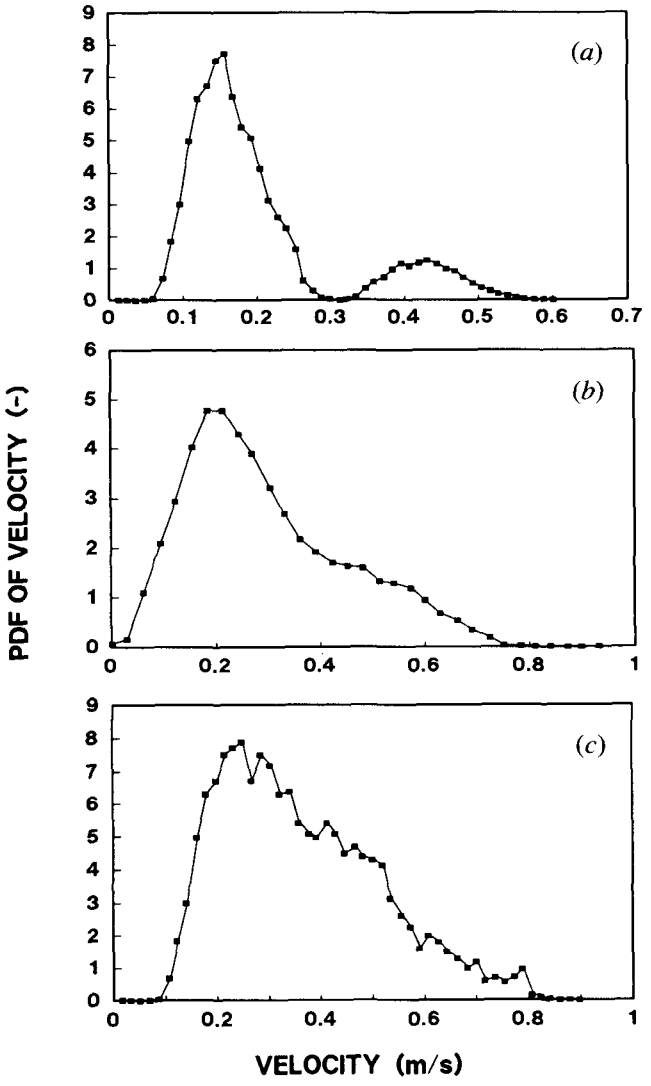

Fig. 1—PDFs of the mixed two-phase velocities: (*a*) was obtained with a fritted glass bubbler; the bubble size was approximately 3 mm for $Q_g = 5.0 \times 10^{-6}$ Nm^3/s; (*b*) was obtained from a chain of bubbles where bubble size was about 7 mm for $Q_g = 7.75 \times 10^{-6}$ Nm^3/s; (*c*) was obtained from a large bubble plume with bubble sizes ranging from 4 to 40 mm for $Q_g = 1.0 \times 10^{-4}$ Nm^3/s.

III. APPARATUS

Two vessels were used for the investigation. The first was a 1/10 scale model of a steelmaking ladle, as shown schematically in Figure 2. The model consisted of a 500-mm-diameter acrylic cylinder 760-mm high, inside an outer box 560 × 560 mm^2 × 760-mm high. The depth of water in the model was 420 mm. Both the cylinder and the outer box were filled with water to minimize distortion due to curvature of the cylinder. Five horizontal slots were cut on the inner cylinder wall to eliminate the curvature effect for lateral velocity measurements at those five planes; the slots were 3-mm high and one quarter of the cylinder circumference long. (Slots not in use were taped closed.) Two types of injectors were used. A glass lance with fritted glass at the end was used to produce small bubbles, 0.5- to 4-mm diameter. Larger bubbles (approximately 5- to 40-mm diameter) were produced by a flush-mounted orifice (4-mm inner diameter) located at the center of the bottom. Most of the work

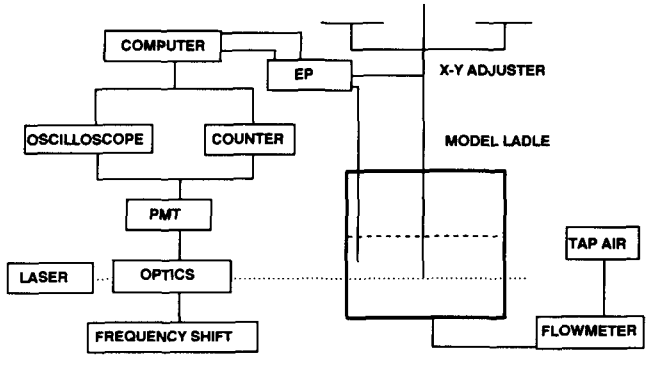

Fig. 2—Illustration of the experimental setup.

was performed with the later injector, except where specifically noted. The vessel was filled with distilled water. Market rice powder was used as seeding for the LDA measurement of liquid velocities.

The other vessel was a smaller PLEXIGLASS* box (100 × 100 mm^2 × 150-mm high) which was used for low flow rates. The box was filled with distilled water to a height of 125 mm. A 4-mm inside diameter copper tube placed 25 mm above the bottom was used as an injector. This vessel was used for low flow rates only (0.5 to 20 ml/s), where individual bubbles follow each other in single file (bubble chains). The bubble sizes range from 5 to 15 mm.

*PLEXIGLASS is a trademark of Rohm & Haas Company, Philadelphia, PA.

The LDA used in this work was DANTEC Model 127 (He-Ne) with a power of 60 mW, which could be used either for forward or backward scattering. The focal lengths of the objective lenses were 80 and 310 mm. The layout of the equipment is shown in Figure 2.

A DISA 55L90a counter was used to process the LDA data. Two operational modes were used: fixed and combined. Under fixed mode operation, data are taken whenever a signal is validated, whereas only one datum is taken from one signal burst in the combined mode. Since a signal burst usually contains many more fringes than required for velocity validation, more velocity data can be obtained under the fixed mode. There are also two modes for the operation of the LDA interface to the computer: timer and LDA. In the timer mode, data are taken at a preset time interval. However, in the LDA mode, the "data ready" command is enabled by a validated signal itself; thus, data are taken as rapidly as possible.[14] The timer mode is very convenient for analog data acquisition (in conjunction with the electrical probe), while for the purpose of the velocity measurement, the LDA mode is usually used.

The construction of the electrical probe tip used in this experiment is shown in Figure 3. When the probe tip is enclosed by a bubble, there is a large change of voltage in the measuring circuit compared to when the tip is in water; thus, bubbles are easily identified. To increase sensitivity, a bridge circuit was developed. The probe signals were collected by the same analog/digital (A/D) interface as the LDA signals; thus, it operated in either the timer or LDA mode described above. The data acquisition rate could be up to 140 kHz. The probe was bent into a "dog leg" shape so that the tip could be positioned less than 1 mm below the LDA focus without interrupting the beam.[13]

To determine the bubble drag coefficients, bubble sizes and velocities were measured from video recordings taken simultaneously with liquid velocity measurements from the LDA.

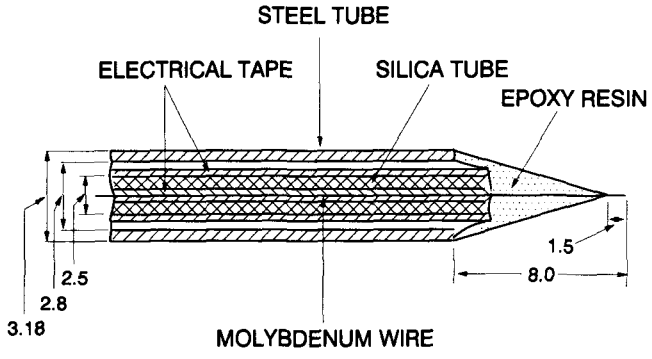

Fig. 3—Structure of electrical probe. The molybdenum wire (0.5-mm diameter) was wrapped with electrical tape and then inserted into a silica tube. The silica tube was, in turn, wrapped with the electrical tape and then inserted into a steel tube. The probe tip was sealed with liquid epoxy resin, leaving 1.5-mm wire exposed. Dimensions are in millimeters.

IV. EXPERIMENTAL RESULTS

Both back scattering and forward scattering were investigated. The back-scattering configuration was found to be best to obtain simultaneous gas and liquid velocities. When the laser measurement volume intersected the bubble interface, strong interference fringes were created. These were more easily observed by back scattering, because the photomultiplier tube was on the same side of the bubble as the fringes. Bubbles not in the measurement volume could disrupt either laser beam, resulting in no data; there were fewer of these events in the back-scattering configuration. A typical time series for the data in back-scattering operation are shown in Figure 4 for both the LDA and the EP.

A. *Liquid Velocity Measurements*

The mean liquid velocities and their fluctuating components were calculated with the conventional equations:

$$U = \frac{1}{N_l} \sum_{i=1}^{N_l} u_i \qquad [1]$$

$$u' = \sqrt{\frac{1}{N_l - 1} \sum_{i=1}^{N_l} (u_i - U)^2} \qquad [2]$$

where N_l is the number of the liquid velocity data.

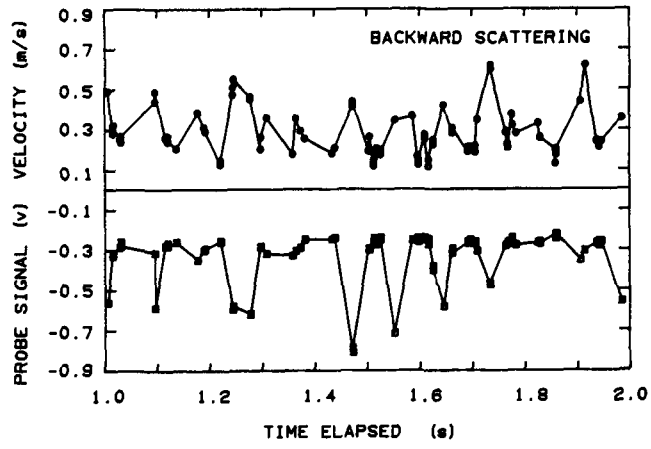

Fig. 4—Signals from LDA/EP. Time series of velocity (upper) and EP voltage (lower) produced in the backward-scattering configuration. This experiment was performed in the small vessel with the 4-mm-diameter nozzle. The LDA was operated under the combined/LDA mode. Q_g = 7.75 × 10^{-6} Nm^3/s, U_b = 0.44 m/s, α = 0.38, f_b = 15/s, and D_b = 9.96 mm.

Different gas flow rates, Q_g, varying from 50 to 200 ml/s were used in the large vessel; typical results with 100 ml/s are presented. The variation of the mean and fluctuating components of the upward liquid velocity along the centerline of the vessel are shown in Figure 5. In the lower regions, liquid entrained from outside the plume is accelerated; 100 mm above the bottom, the liquid starts to slow due to expansion of the plume and breakup of the bubbles. Near the free surface, upward flow of liquid is restricted by the free surface.

The mean and fluctuating liquid velocity flow fields are shown in Figures 6 and 7, respectively. The mean liquid flow field (Figure 6) reveals that the flow inside the two-phase plume zone is much faster than the flow in the single-phase region. The velocity decays significantly along the radial direction due to the rapid decline of the void fraction along the radial direction. Along the side walls, the downward flow is still strong. However, in the region close to the bottom wall, the flow is slow, and a stagnant zone may exist. The turbulent components of the velocity shown in Figure 7 are also much stronger in the two-phase region. The angle of the turbulent velocity vectors from the horizontal is given by

$$\theta_t = \text{arctg}\,(u'/v') \qquad [3]$$

If the turbulence is isotropic, the angle is 45 deg; however, the angle is approximately 55 deg, decreasing slightly with increasing flow rate, as shown in Figure 8.

B. *Bubble Velocity Measurements*

The mean bubble velocities and fluctuating components were calculated once the bubble velocities were separated from the mixed velocity sample. Expressions analogous to Eqs. [1] and [2] were employed. Figure 9 shows the vertical bubble velocities along the centerline of the vessel taken at the same time as the liquid velocities in Figure 5. The bubble velocities are obtained when a bubble interface crosses the laser measurement volume; thus, the bubble velocities are the interfacial velocities. The root mean square (RMS) velocity in the

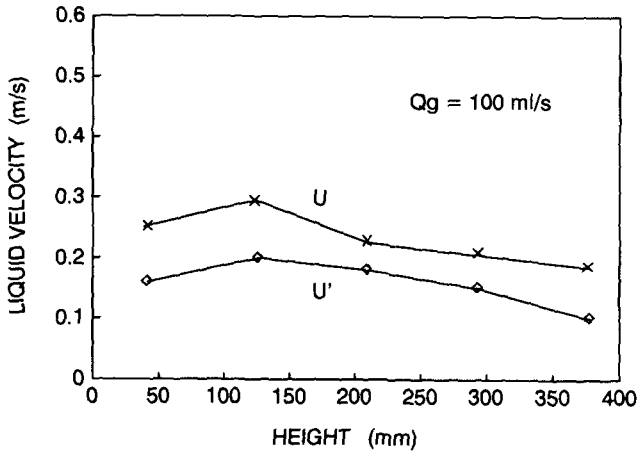

Fig. 5—Mean and RMS component of the liquid velocity variation along the centerline of the plume. Result from the bubbly plume produced with the flush-mounted nozzle at Q_g = 100 ml/s.

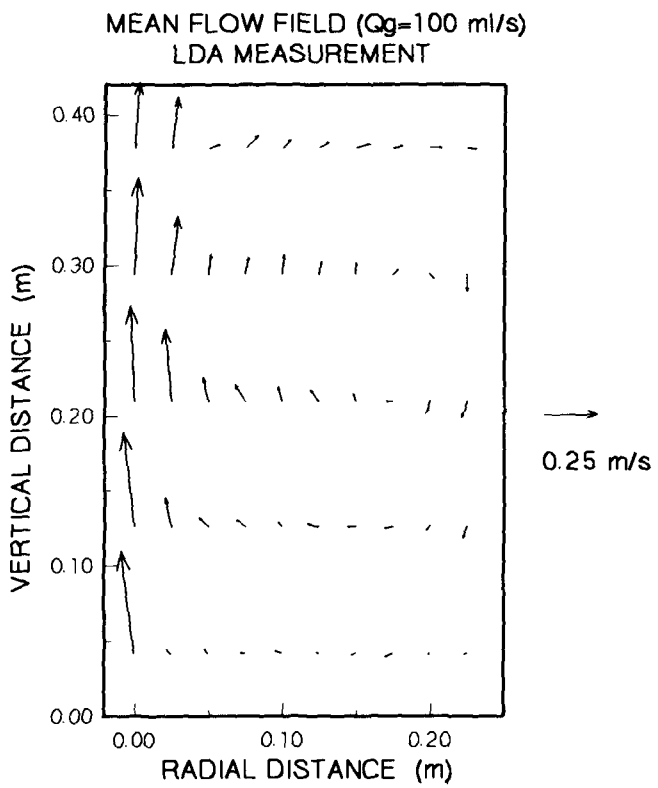

Fig. 6—Flow pattern of the mean liquid velocities in the model ladle produced with the flush-mounted nozzle at Q_g = 100 ml/s.

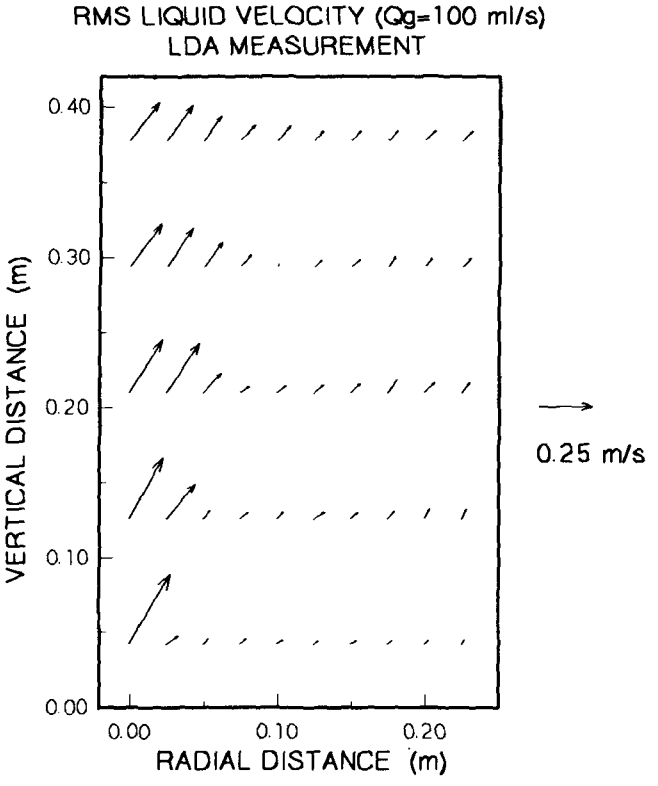

Fig. 7—Distribution of the RMS component of the liquid velocity in the model ladle for the same conditions as Fig. 6.

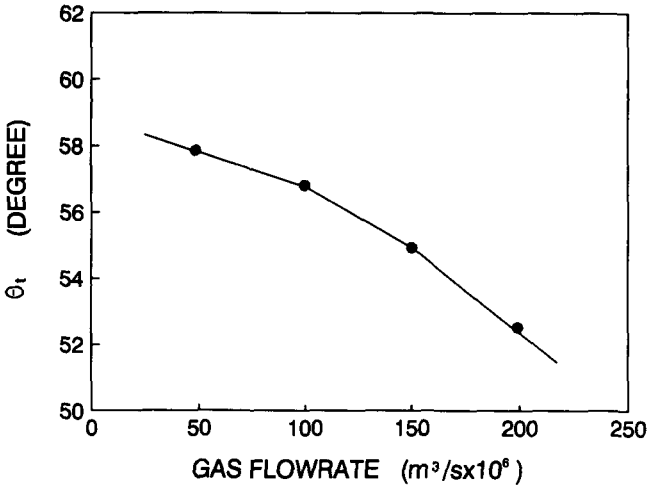

Fig. 8—Variation of turbulence angle; defined by Eq. [3].

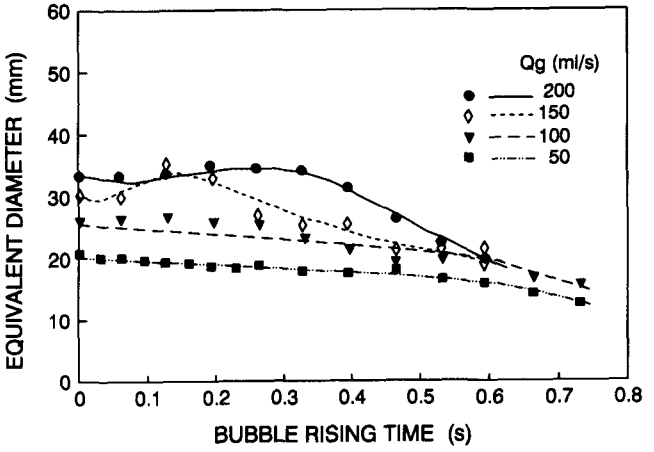

Fig. 10—Equivalent diameter of bubbles along the centerline of the plume produced with the flush-mounted nozzle for various flow rates. Measurements were made from video recordings.

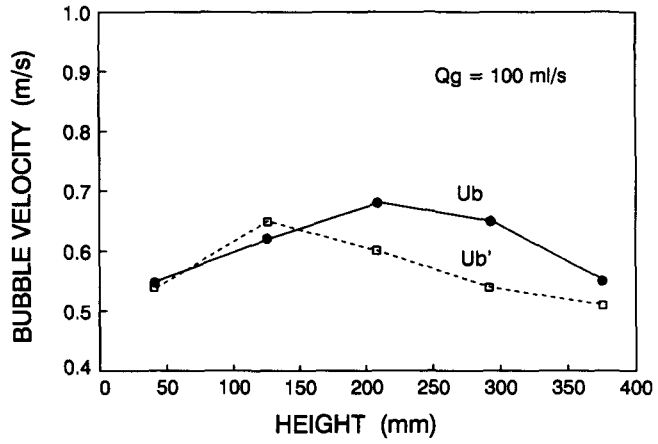

Fig. 9—Mean and RMS component of the bubble velocity along the centerline of the plume produced with the flush-mounted nozzle in the large vessel at Q_g = 100 ml/s.

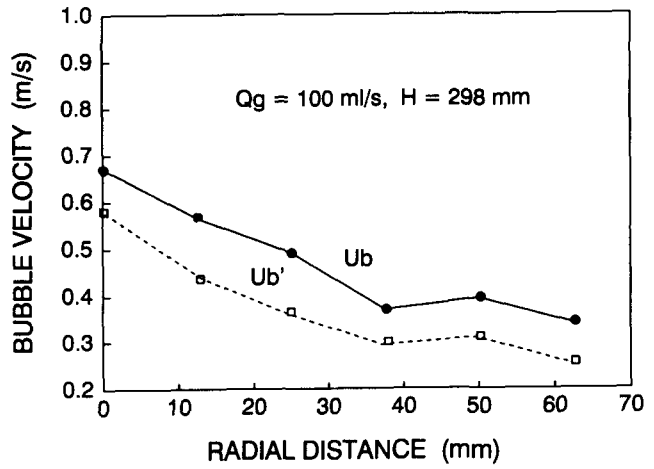

Fig. 11—Radial distribution of the mean and the RMS component of the bubble velocities in a plume produced with the flush-mounted nozzle for Q_g = 100 ml/s. The data were taken from a plane 298 mm above the model bottom.

vertical direction is primarily due to wobbling of the individual bubble interfaces, rather than a spectrum of rising velocities. The wobbling is readily apparent from visual observation of the bubbles. Figure 9 shows that immediately after detachment, the bubbles accelerate rapidly and oscillate dramatically; the RMS value of the bubble velocity is comparable to the rising velocity. These fluctuations decrease as the bubbles rise but are always more than half of the mean rising velocity.

From video measurement of bubble size in the plume, it was determined that the bubbles break up. The bubble size during rise is shown in Figure 10, where the volume equivalent bubble diameter is obtained by measuring the chord length and height of these spherical cap bubbles with a video camera and assuming that the base of the bubble is circular. The decrease in bubble size with rising time may partially account for the decrease in the mean velocity of the bubbles. As shown in Figure 5, the liquid is also moving more slowly at this point.

Along the radial direction, the variation of the bubble velocity reveals other characteristics of the bubble behavior (Figure 11). In the center of the plume, bubbles rise with much higher velocity than those away from the plume center because larger bubbles rise in the center of the plume. Bubble equivalent diameters are several times smaller on the outer edges of the plume, as shown in Figure 12. The rapid decay of the bubble rising velocity along the radial direction also reflects the decreasing upward liquid flow along the radial direction.

C. *Distribution of the Void Fraction*

The distribution of void fraction obtained with the electrical probe measurement is shown in the form of a contour map for gas flow rate of 100 ml/s in Figure 13. The radial variations of the void fraction are similar to the Gaussian distribution, as observed by many researchers.[5,6,15,16]

D. *Distribution of the Turbulent Kinetic Energy*

The turbulent kinetic energy of the liquid, k, can be calculated from the RMS values of the liquid velocity

components shown in Figure 7 using the following equation:

$$k = \frac{1}{2}(u'^2 + v'^2 + w'^2) \quad [4]$$

where u' and v' were measured with the LDA/EP technique and w' is assumed to be equal to v' at the same location in the flow. The resulting distribution of k is shown in Figure 14 for a gas flow rate of 100 ml/s. The magnitude of the turbulence in the two-phase zone is significantly greater than that in the single-phase area, which reflects the strong effect of bubble movement on the turbulence in the liquid phase. The strongest turbulence appears immediately above the nozzle.

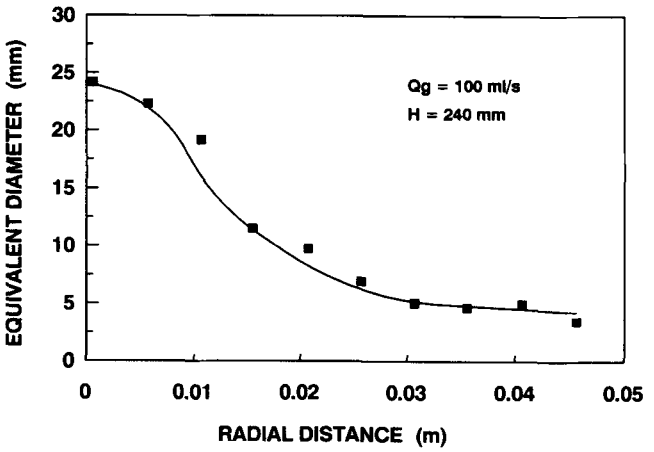

Fig. 12—Equivalent diameter of bubble across the plume 240 mm from the ladle bottom. The plume was produced with the flush-mounted nozzle for Q_g = 100 ml/s.

V. DISCUSSION

A. *Relative Velocities and Drag Coefficients of Bubbles*

The bubbles can be conveniently divided into three groups, according to the manner in which they were formed. The bubbles produced with the fritted glass in the larger tank were smallest (Figure 15(a)). Intermediate-sized bubbles were produced in a bubble chain by the injector at low gas flow rates in the smaller vessel (Figure 15(b)). The largest bubbles were obtained from the flush-mounted injector in the larger tank at higher gas flow rates (Figure 15(c)).

Bubble diameters were estimated from video recordings of the bubbles; thus, it is possible to determine the drag coefficients of the bubbles in the plumes according to

$$C_D = \frac{2F_B}{\rho U_r^2 A_B} \quad [5]$$

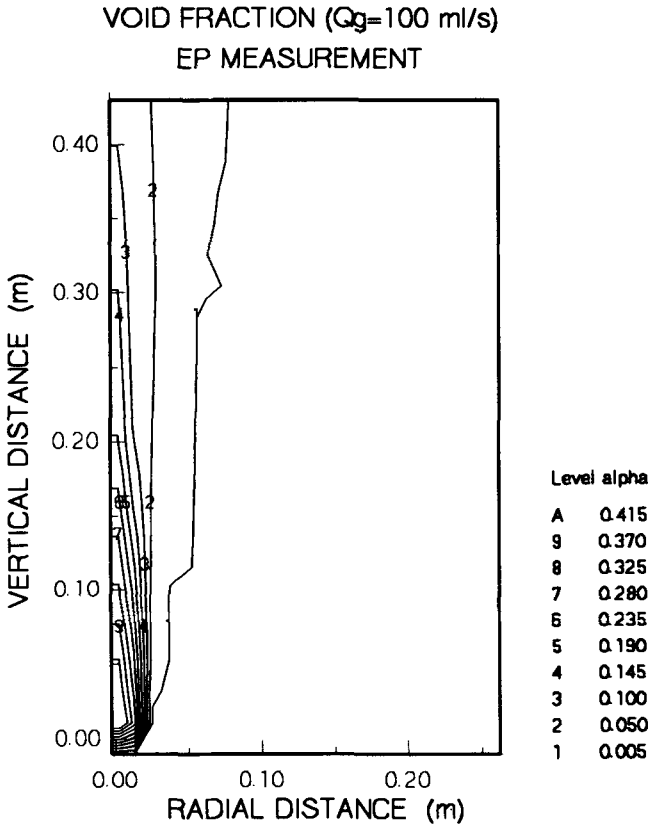

Fig. 13—Contour map of the distribution of the void fraction in the large vessel produced with the flush-mounted nozzle for Q_g = 100 ml/s.

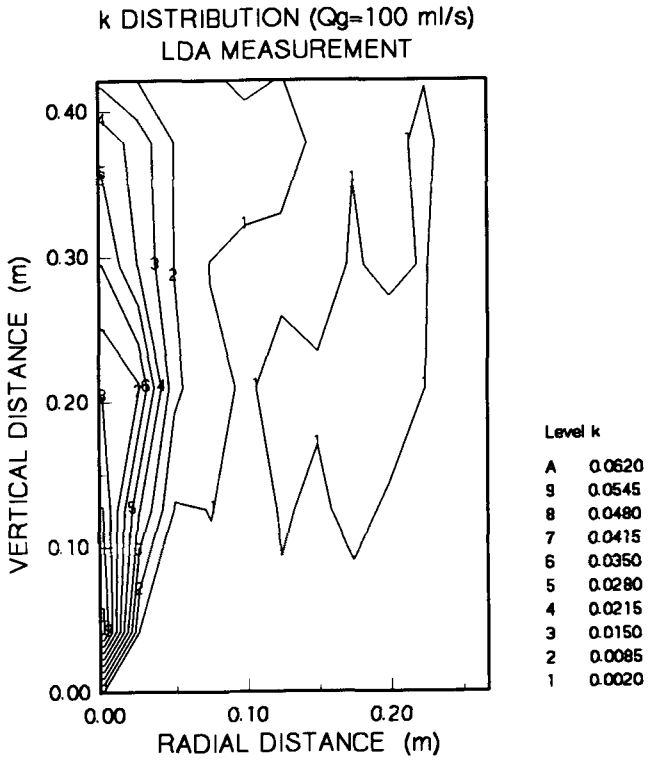

Fig. 14—Contour map of the distribution of the turbulent kinetic energy in the large vessel produced with the flush-mounted nozzle for Q_g = 100 ml/s.

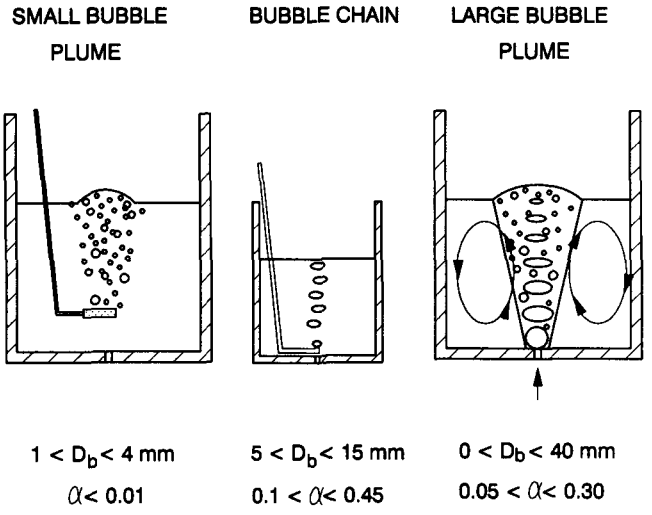

Fig. 15—Illustration of the three injection configurations.

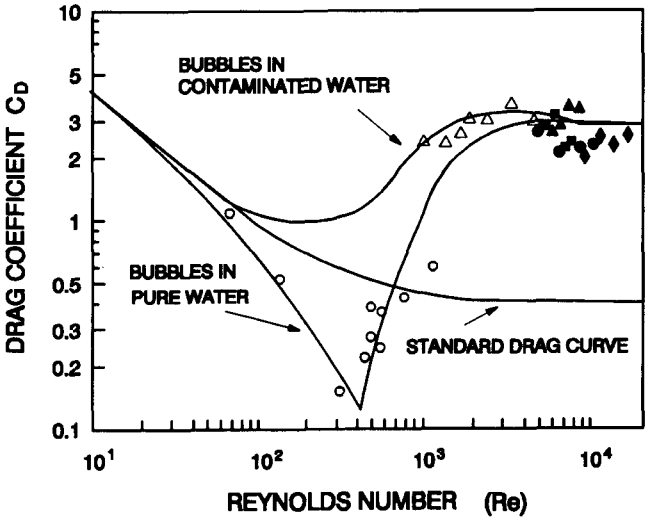

Fig. 16—Variation of drag coefficient with the bubble Reynolds number. The three groups of data were obtained from the three measurement configurations shown in Fig. 15. (○) Small bubble plumes; (△) bubble chains; (●) large bubble plumes, H = 378 mm; (■) large bubble plumes, H = 294 mm; (▲) large bubble plumes, H = 210 mm; and (◆) large bubble plumes, H = 126 mm.

where the body force is taken as bubble buoyancy:

$$F_B = V_B(\rho_l - \rho_g)g \qquad [6]$$

Other forces due to the acceleration of the bubble added mass, and history terms are small compared to the buoyancy. The acceleration of bubbles in the plume is typically less than 0.1 m/s^2. Consequently, added mass forces are less than 1 pct of the buoyancy force due to gravitational acceleration (9.81 m/s^2). For these drag coefficient measurements, the bubble velocity was obtained from the video measurements along with the bubble size, while the liquid velocity was acquired from the LDA. The drag coefficients are plotted as a function of Reynolds number in Figure 16. The standard drag curve for spheres and drag coefficients for bubbles in pure and contaminated water are also shown for comparison.[17] In the present apparatus, bubble size and void fraction depend on flow rate and position in the vessel. These relationships are shown in Figure 17 for both the small and large vessels. The void fraction in the small bubble plume produced with the fritted glass was less than 1 pct and, therefore, not included in Figure 17. Comparison of Figures 16 and 17 shows that the drag coefficient is only weakly dependent on void fraction. It is very surprising that there is such good agreement between the single bubble drag coefficients and those in the two experimental systems at high void fractions and high levels of turbulence. It should be noted that distilled water was used for the small bubble plume in the small vessel, while seeding was used in the larger vessel. For the bubbles produced in distilled water with the fritted glass at low void fraction (<0.02), the data (circles in Figure 16) are almost identical to the single bubble data for pure water. The bubbles in the bubble chain in distilled water (triangles in Figures 16 and 18) had drag coefficients higher than for bubbles in pure water. This discrepancy may be due to the high void fraction and short distance between the measuring position and the nozzle, which limited the full acceleration of the bubble. The largest bubbles (solid points in Figures 16 and 17) had drag coefficients close

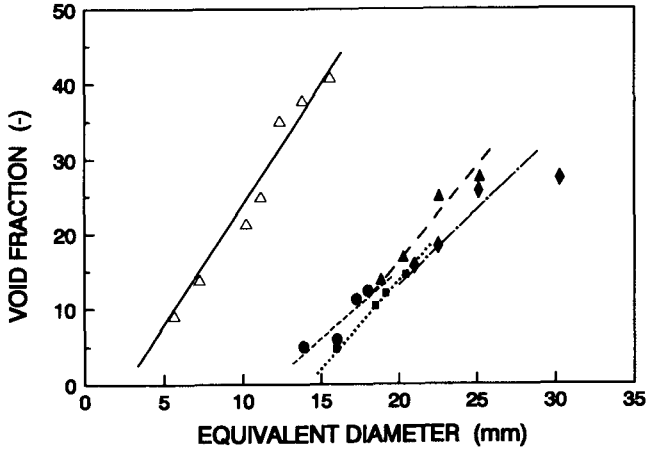

Fig. 17—Time-averaged local void fractions for the data in Figs. 16 and 18. (The void fraction in the small bubble plume produced with the fritted glass was less than 1 pct and therefore not included.) (△) Bubble chains; (●) large bubble plumes, H = 378 mm; (■) large bubble plumes, H = 294 mm; (▲) large bubble plumes, H = 210 mm; and (◆) large bubble plumes, H = 126 mm.

to the single bubble values, but there was more scatter in the data. The mean values of the drag coefficient are in reasonably good agreement with those of a single bubble.

The data are replotted in Figure 18 to show the relationship between the relative velocity and equivalent diameter and to compare it with the curves from Clift *et al.*,[17] which summarize the terminal rising velocities of single bubbles in stagnant water. The range of void fractions can be taken from the companion diagram (Figure 17). The above experimental results suggest that the relative velocity of bubbles in a bubbly plume can be well represented by the terminal velocity of a single bubble.

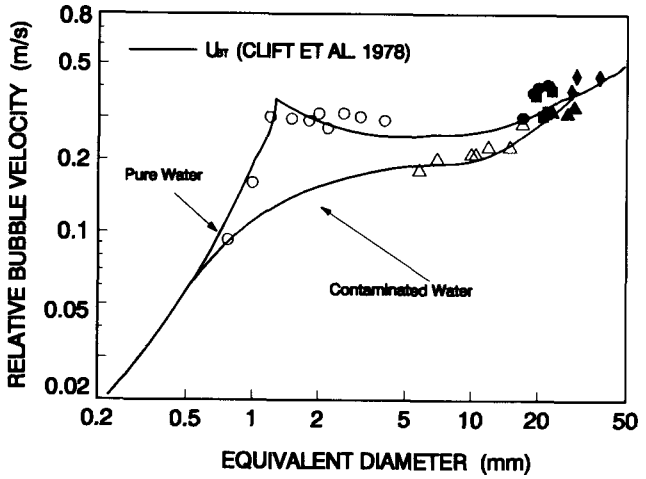

Fig. 18—Variation of drag coefficient with the equivalent bubble diameter from the same data as Figs. 16 and 17. (○) Small bubble plumes; (△) bubble chains; (●) large bubble plumes, H = 378 mm; (■) large bubble plumes, H = 294 mm; (▲) large bubble plumes, H = 210 mm; and (◆) large bubble plumes, H = 126 mm.

This is the first time that the slip velocities of bubbles in plumes relevant to ladle metallurgy have been measured. A variety of simplifying assumptions have been used for plume velocities. The earliest approach was also the simplest: no slip between the two phases.[18] The terminal velocity for a single bubble of one size has been used most often to represent the relative velocity of the entire bubble phase.[19,20,21] The present experimental results demonstrate that there is a range of bubble sizes due to breakup. At any instant, the slip velocity of particular bubbles is close to the velocity of a single bubble of the same size rising in stagnant liquid. In order to simplify mathematical modeling, it is not unreasonable to assume that bubbles of one size rise with slip velocities similar to single bubble rising velocities.

More recently, Johansen and Boysan have adopted a Lagrangian frame of reference to track individual bubbles through the turbulent flow.[22] In this model, the relative velocities of bubbles were calculated based on the drag coefficient model originally proposed by Ishii and Zuber,[23] which takes the following form:

$$C_{D\alpha} = C_D(1 - \langle\alpha\rangle)^b \qquad [7]$$

where $C_{D\alpha}$ is the drag coefficient on bubbles in the two-phase flow with an average void fraction of $\langle\alpha\rangle$, C_D is the standard drag coefficient for single bubbles in stagnant fluid, and b is a constant assuming a value of 1 for bubbly pipe flow and 2 for bubbly churn flow. For a void fraction of 0.25, the drag coefficient is reduced by between 25 and 44 pct, depending on the value of b. Clearly, this is not the case in Figure 18. It is important to note that the void fraction measured by Ishii and Zuber was cross-sectional averaged, rather than the local values as measured in this experiment. The cross-sectional averaged void fractions in this experiment would be much lower than those measured by Ishii and Zuber.

Ishii and Zuber[23] developed Eq. [7] for a gas-liquid pipe flow. It was assumed that the pressures in the liquid and the gas phases were the same so that the mixture pressure drop could be calculated with a momentum balance of only the gas phase, while the other momentum losses in the liquid phase could be neglected. The drag between the gas and liquid was calculated by simply summing the drag forces on all of the bubbles inside the control volume. When bubble density is high in a pipe flow and the boundary layers of these bubbles are overlapping, both phases may be approximated as continua, and the above assumptions may hold. In an unconfined plume, the vertical pressure drop is more appropriately given by the hydrostatic head in the liquid. Thus, the calculation of pressure drop based only on a momentum balance in the gas phase is not applicable.

The above discussion implies that the model of Ishii and Zuber[23] may only be applied to confined bubbly flows with rather small bubbles and dense bubble populations. For the bubbly plume flows encountered in the present study, the bubbles should be treated as individual bubbles, and the relative velocity with respect to the liquid flow around the bubble can be better predicted using the terminal velocity rather than using the model of Ishii and Zuber.

B. *Turbulence Characteristics*

In most single-phase flows, the turbulence intensity is usually less than 0.2. However, in bubbly plume, the turbulence intensity of the liquid flow can be greater than 0.5, as shown in Figure 5. The movement of bubbles contributes a great deal to the generation of the turbulence in the two-phase region simply by their motion but also through interfacial interactions, such as the wake shedding and wobbling motion. Wake shedding and wobbling involve the transfer of energy from the gaseous phase to the liquid phase in an unsteady manner; thus, they contribute to liquid turbulence. Larger bubbles have more momentum and more violent interface wobbling; therefore, they tend to generate more turbulence than smaller bubbles. This may be shown with the radial decay of turbulence intensity as measured in this experiment (Figure 11). Turbulence is strongest in the plume center where bubbles are largest and decays in the radial direction in a similar way as the decay of bubble size (Figure 12).

It has usually been assumed that the turbulence is isotropic so that the k-ε model can be employed to model flow in ladles; however, this assumption has never been justified. The present results in Figures 7 and 8 indicate that θ_t is approximately 55 deg rather than 45 deg for isotropic flow. If one assumes that the tangential component is equal to the radial one, the turbulent kinetic energy, k, can be calculated, as shown in Figure 14. The assumption of completely isotropic turbulence would result in values 30 to 50 pct higher. Thus, the assumption of isotropic turbulence is a reasonable assumption within these limits.

Some insight into nonisotropy can be gained with turbulence theory. Turbulence in single-phase flow is generated by the viscous shear forces, which, in turn, are the results of the mean velocity gradient. Using the

Einstein convention, the time-averaged turbulent energy budget assumes the following form:[24,25]

$$U_j \frac{\partial}{\partial x_j}\left(\frac{1}{2}\overline{u_i' u_i'}\right) = -\frac{\partial}{\partial x_j}\left(\frac{1}{\rho}\overline{u_j' p} + \frac{1}{2}\overline{u_i' u_i' u_j'} - 2\nu\overline{u_i' s_j}\right) - \overline{u_i' u_j'} S_{ij} - 2\nu\overline{s_{ij} s_{ij}} \quad [8]$$

where

$$s_{ij} \equiv \frac{1}{2}\left(\frac{\partial u_i'}{\partial x_j} + \frac{\partial u_j'}{\partial x_i}\right) \quad [9]$$

and

$$S_{ij} \equiv \frac{1}{2}\left(\frac{\partial U_i}{\partial x_j} + \frac{\partial U_j}{\partial x_i}\right) \quad [10]$$

The subscripts 1 through 3 indicate x, r, and θ directions, respectively. If one assumes that the flow is dominated by flow in the axial, x, direction, then one can ignore U_j and $\partial U_i/\partial x_j$, except for U and $\partial U/\partial r$. Taking the velocities in the x, r, and θ directions as U, V, and W, respectively, the turbulent energy balances in the same three respective directions can be simplified to

$$O = -\overline{u'v'}\frac{\partial U}{\partial r} + \frac{1}{\rho}\overline{p\frac{\partial u'}{\partial x}} - \frac{\partial}{\partial r}\overline{\frac{1}{2}u'^2 v'} - \frac{1}{3}\varepsilon \quad [11]$$

$$O = O + \frac{1}{\rho}\overline{p\frac{\partial v'}{\partial r}} - \frac{\partial}{\partial r}\overline{\left(p/\rho + \frac{1}{2}v'^2\right)v'} - \frac{1}{3}\varepsilon \quad [12]$$

$$O = O + \frac{1}{\rho}\overline{p\frac{\partial w'}{\partial \theta}} - \frac{\partial}{\partial r}\overline{\frac{1}{2}w'^2 v'} - \frac{1}{3}\varepsilon \quad [13]$$

The only turbulent production term is the first one on the right-hand side of Eq. [11]; there is no generation of turbulence in the r and θ directions. They can only acquire kinetic energy from the nonlinear pressure-velocity interactions.[24,25] This argument also implies that larger velocity gradients along a particular direction would produce more turbulence and skew it toward that direction. However, it should also be noted that turbulent kinetic energy tends to break up large eddies which are more likely to cause the nonisotropy, so that isotropy would be improved by pressure-velocity interactions. The measured θ_t for four different gas flow rates are shown in Figure 8, where the degree of nonisotropy decreases with increasing gas flow rate. This observation qualitatively supports the above argument.

Equations [12] and [13] may also be used to estimate the turbulence level in the horizontal directions. Since in these directions the turbulence is developed in a similar way through the pressure-velocity interaction, it is likely that v' and w' are at the same level. Some experimental measurement of turbulence in developed pipe flow[26] and in a self-preserving jet[27] seems to support this argument. As a result, it should be reasonable to assume that the turbulence intensity is isotropic in the horizontal directions for the calculation of k, as shown in Figure 14.

VI. CONCLUSIONS

A combined laser Doppler and EP technique was applied to the study of gas plumes in water to simulate ladle metallurgy practice. The experimental results reveal that:

1. The relative velocity of bubbles in an unconfined plume, as well as in a chain of bubbles, is not affected by the void fraction. Therefore, the slip velocity of the bubbles is within about 10 pct of the velocities of single bubbles rising in stagnant liquid. Ishii and Zuber's correlation[23] for rising velocity cannot be applied to the situations discussed in this work.
2. The intensity of turbulence in the two-phase plume region is generally greater than 0.5 due to the strong interaction between the liquid and gas phases.
3. The turbulence in the plume region is not completely isotropic; it is slightly skewed to the vertical direction. The isotropic assumption results in errors of the order of 30 to 50 pct in the calculation of turbulent kinetic energy. The anisotropy of turbulence is a result of the fact that the shear in the vertical direction is much greater than in any other directions. Furthermore, the anisotropy is weakened with the greater input of energy into the system.

NOMENCLATURE

C_D	drag coefficient of a single bubble
$C_{D\alpha}$	drag coefficient of bubbles at void fraction α
D_B	volume equivalent diameters of bubble
F_D	drag force on a bubble
H	height from the bottom of the water model
k	turbulent kinetic energy
Q_g	gas flow rate
p	pressure
Re	Reynolds number, $UD_B\rho/\mu$
x, r, θ	vertical, radial, and angular coordinates
t	bubble transient time
U, V, W	mean liquid velocity components
u', v', w'	turbulent components of liquid velocities
U_B, u_B'	mean and turbulent components of bubble rising velocities
U_r	relative velocity between the liquid and bubbles
α	time mean void fraction
θ_t	angle defined by Eq. [3]
ρ	liquid density
μ	liquid viscosity
ε	dissipation of kinetic energy

ACKNOWLEDGMENTS

The kind cooperation of Dr. P.E. Wood during the experiments which were carried out in his laboratory and fruitful discussions with Dr. O. Turan during the writing

of this article are greatly appreciated. Financial support by the Canadian International Development Agency and the Natural Sciences and Engineering Research Council is gratefully acknowledged.

REFERENCES

1. M. Sano and K. Mori: *Trans. Iron Steel Inst. Jpn.*, 1980, vol. 20, pp. 668-73.
2. M. Sano and K. Mori: *Trans. Iron Steel Inst. Jpn.*, 1980, vol. 20, pp. 674-85.
3. M. Sano and K. Mori: *SCANINJECT III, Mefos and Jernkontoret*, Lulea, Sweden, 1983, pp. 6:1-17.
4. M. Kawakami, Y. Kitazawa, T. Nakamura, T. Miyake, and K. Ito: *Trans. Iron Steel Inst. Jpn.*, 1985, vol. 25, pp. 394-402.
5. A.H. Castillejos and J.K. Brimacombe: *Metall. Trans. B*, 1987, vol. 18B, pp. 649-58.
6. A.H. Castillejos and J.K. Brimacombe: *Metall. Trans. B*, 1987, vol. 18B, pp. 659-71.
7. D. Mazumdar and R.I.L. Guthrie: *Metall. Trans. B*, 1985, vol. 16B, pp. 83-90.
8. D. Mazumdar and R.I.L. Guthrie: *Ironmaking and Steelmaking*, 1985, vol. 12 (6), pp. 256-64.
9. J.H. Grevet, J. Szekely, and N. El-Kaddah: *Int. J. Heat Mass Transfer*, 1982, vol. 25 (4), pp. 487-97.
10. F. Oeters, H.C. Dromer, and J. Kepura: *Mefos and Jernkontoret, SCANINJECT II*, 1983, Lulea, Sweden, pp. 7:1-7:22.
11. P.E. Anagbo and J.K. Brimacombe: *Metall. Trans. B*, 1990, vol. 21B, pp. 637-48.
12. S.T. Johansen, D.G.C. Robertson, K. Woje, and T.A. Engh: *Metall. Trans. B*, 1988, vol. 19B, pp. 745-54.
13. Y.Y. Sheng and G.A. Irons: *Int. J. Multiphase Flow*, 1991, vol. 17 (5), pp. 585-98.
14. C. Tropea and D. Struthers: *Proc. Conf. Use of Computers in Laser Velocimetry*, Deutsche-Franzosisches Forschungs Institute, Saint-Louis, Senegal, May 18–20, 1987.
15. K.-H. Tacke, H.-G. Schubert, D.J. Weber, and K. Schwerdtfeger: *Metall. Trans. B*, 1985, vol. 16B, pp. 263-75.
16. M.A.S.C. Castello-Branco and K. Schwerdtfeger: Presented at the 26th Annual Conference of Metallurgists, Winnipeg, Canada, 1987, p. 30.
17. R. Clift, G.R. Grace, and M.E. Weber: *Bubbles, Drops and Particles*, Academic Press, New York, NY, 1978.
18. J. Szekely, H.J. Wang, and K.M. Kiser: *Metall. Trans. B*, 1976, vol. 7B, pp. 287-95.
19. T. DebRoy, A.K. Majumdar, and D.B. Spalding: *Appl. Math. Modelling*, 1978, vol. 2, pp. 146-50.
20. M. Salcudean, K.Y.M. Lai, and R.I.L. Guthrie: *Can. J. Chem. Eng.*, 1985, vol. 63, pp. 51-61.
21. L.R. Farias and G.A. Irons: *Metall. Trans. B*, 1986, vol. 17B, pp. 77-85.
22. S.T. Johansen and F. Boysan: *Metall. Trans. B*, 1988, vol. 19B, pp. 755-64.
23. M. Ishii and N. Zuber: *AIChE J.*, 1979, vol. 25 (5), pp. 843-55.
24. H. Tennekes and J.L. Lumley: *A First Course in Turbulence*, The MIT Press, Cambridge, MA, 1972.
25. J.Q. Hinze: *Turbulence*, 2nd ed., McGraw-Hill, New York, NY, 1975.
26. C.J. Lawn: *J. Fluid Mech.*, 1971, vol. 48, Part 3, pp. 477-505.
27. I. Wygnanski and H. Fiedler: *J. Fluid Mech.*, 1969, vol. 38, Part 3, pp. 577-612.